Ioannis Goulos[1]
Propulsion Aerodynamics and
Performance Engineering,
Centre for Propulsion and Thermal
Power Engineering,
School of Aerospace,
Transport and Manufacturing,
Cranfield University,
Bedfordshire MK43 0AL, UK
e-mail: i.goulos@cranfield.ac.uk

David MacManus
Gas Turbine Technology Group,
Centre for Propulsion and Thermal
Power Engineering,
School of Aerospace,
Transport and Manufacturing,
Cranfield University,
Bedfordshire MK43 0AL, UK
e-mail: D.G.Macmanus@cranfield.ac.uk

Josep Hueso Rebassa
Propulsion Aerodynamics,
Centre for Propulsion and Thermal
Power Engineering,
School of Aerospace,
Transport and Manufacturing,
Cranfield University,
Bedfordshire MK43 0AL, UK
e-mail: J.Hueso-Rebassa@cranfield.ac.uk

Fernando Tejero
Propulsion Systems Design,
Centre for Propulsion and Thermal
Power Engineering,
School of Aerospace,
Transport and Manufacturing,
Cranfield University,
Bedfordshire MK43 0AL, UK
e-mail: F.Tejero@cranfield.ac.uk

Andy Au
Aircraft Research Association Ltd.,
Manton Lane,
Bedford, Bedfordshire MK41 7PF, UK
e-mail: andycheau@gmail.com

Christopher Sheaf
Installation Aerodynamics,
Rolls-Royce plc,
P.O. Box 31,
Derby DE24 8BJ, UK
e-mail: Christopher.Sheaf@Rolls-Royce.com

Impact of Installation on the Performance of an Aero-Engine Exhaust at Wind-Milling Flow Conditions

This paper presents a numerical investigation of the effect of wing integration on the aerodynamic behavior of a typical large civil aero-engine exhaust system at wind-milling flow conditions. The work is based on the dual stream jet propulsion (DSJP) test rig, as will be tested within the transonic wind tunnel (TWT) located at the aircraft research association (ARA) in the UK. The DSJP rig was designed to measure the impact of the installed pressure field due to the effect of the wing on the aerodynamic performance of separate-jet exhausts. The rig is equipped with the dual separate flow reference nozzle (DSFRN), installed under a swept wing. Computational fluid dynamic simulations were carried out for representative ranges of fan and core nozzle pressure ratios (CNPR) for "engine-out" wind-milling scenarios at end of runway (EOR) takeoff, diversion, and cruise conditions. Analyses were done for both isolated and installed configurations to quantify the impact of the installed pressure field on the fan and core nozzle discharge coefficients. The impact of fan and core nozzle pressure ratios, as well as freestream Mach number and high-lift surfaces on the installed suppression effect, was also evaluated. It is shown that the installed pressure field can reduce the fan nozzle discharge coefficient by up to 16%, relative to the isolated configuration for EOR wind-milling conditions. The results were used to inform the design and setup of the experimental activity which is planned for 2023. [DOI: 10.1115/1.4063939]

1 Introduction

1.1 Background. Modern trends in civil aviation dictate an increase in propulsive efficiency through a concurrent reduction in specific thrust [1,2]. This is enabled by an increase in bypass ratio, which is typically facilitated with larger fan diameters [3]. This trend is likely to be accompanied with the integration of compact nacelles to reduce the associated nacelle drag and weight penalties [4–6]. However, this increase in nacelle compactness may lead to a greater sensitivity of nacelle drag to the ingested stream-tube mass flow capture ratio under off-design conditions such as wind-milling [7,8]. The engine-ingested mass flow is dependent, among others, on the aerodynamic behavior of the exhaust, and specifically on the fan nozzle discharge coefficient (C_d^{Fan}) [9].

During wind-milling, the engine by-pass ratio is very high with most of the mass flow going through the bypass duct, and minimal flow passing through the core [10,11]. Furthermore, the fan nozzle operates unchoked with very low total to static pressure ratios [10,11]. This renders the mass flow discharged through the fan nozzle highly sensitive to the external static pressure field [12]. As a result, C_d^{Fan} can be sensitive to the effect of the pressure field produced by the airframe in-flight [13]. This effect can be further amplified by the presence of the high-lift surfaces [14,15]. This "installed pressure field" can suppress the fan nozzle mass flow leading to a concurrent reduction in engine ingested mass flow [13]. Hence, it is essential to understand the impact of this "installed pressure field" on the aerodynamic behavior of the exhaust during wind-milling since it affects the engine ingested mass flow and the associated nacelle drag [16].

1.2 Exhaust Performance Metrics. A separate-jet exhaust is designed to accelerate the fan and core flows efficiently to maximize overall gross thrust [17]. The aerodynamic performance of the fan and core nozzles is typically quantified using two nondimensional metrics, namely, the discharge and velocity coefficients, C_d and C_v, respectively [18–20].

The discharge coefficient C_d is defined as ratio of the actual nozzle mass flow over the ideal nozzle mass flow resulting from isentropic flow expansion to ambient static pressure. C_d quantifies the internal losses within the nozzle as well as any flow suppression effects [12,13]. Therefore, C_d accounts for losses due to skin-friction and boundary layer growth along the nozzle walls, throat blockage, and any other loss mechanisms within the nozzle [17]. Moreover, C_d accounts for any changes to the static pressure within which the nozzle exhausts and can suppress the nozzle mass flow. These "suppression effects" can be classified under three categories: (a) "Free-stream suppression," which stems from the impact of freestream flow [21,22], (b) "Installed suppression," which manifests due to the aerodynamic interference of the engine with the airframe [18,19,23], and (c) "fan suppression," which is only pertinent for the core nozzle and is due to the impact of the fan nozzle flow on the core nozzle [21,22].

The velocity coefficient C_v is defined as the ratio of the actual nozzle gross propulsive force over the ideal gross propulsive force, which would result from the actual nozzle mass flows under isentropic expansion. Therefore, C_v quantifies the impact of entropic flow effects that can manifest in the exhaust nozzle and jet. These include skin friction and boundary layer growth within ducts, nozzles, pylon, and after-bodies, as well as viscous shear layers, shock waves, and expansion fans within the jet [12].

1.3 Impact of Installation on Exhaust Performance. The existing literature contains ample references where the impact of installation on the aerodynamic behavior of separate-jet exhausts has been investigated for midcruise conditions. Oliveira et al. [24] outlined the key mechanisms of aerodynamic interaction between the engine and the airframe for a narrow-body twin-engine aircraft. Reynolds-Averaged Navier–Stokes (RANS) computational fluid dynamics (CFD) analyses were carried out for a podded under-wing engine installation. One of the pertinent mechanisms identified was

the formation of a "gully" flow between the wing, pylon, and the core after-body. This "gully" effect resulted in increased local flow acceleration on the core after-body, wing, and pylon. This increased acceleration led to an increase in shock loss. However, the impact of installation on exhaust performance in terms of C_v and C_d was not explicitly quantified by Oliveira et al. [24].

Otter et al. [23] performed a RANS CFD investigation to evaluate the impact of installation on the aerodynamic behavior of two aero-engines across a range of installation positions. Analyses were carried out for two aero-engine architectures with by-pass ratio of 11 and 18, respectively, operating at midcruise. Both engines were installed on the NASA common research model (CRM) [25] in a podded under-wing manner. The fan nozzle was found to be unaffected by the installation effect because it was choked for both engines. This rendered the fan nozzle mass flow insensitive to external static pressure disturbances. However, a variation range of approximately 10% was found for C_d^{Core} across the range of installation positions. This was because the core nozzle was unchoked for both engines and therefore it was more sensitive to installed suppression effects [23]. However, the work of Otter et al. [23] did not account for close coupled installation positions that are pertinent for very high bypass ratio engines. Furthermore, it omitted the effect of the pylon.

Goulos et al. [12] carried out a numerical investigation based on RANS CFD to quantify the impact of installation for a very high bypass ratio aero-engine at midcruise with BPR ≈ 15 installed on the NASA CRM [25]. The work done by Goulos et al. [12] included close coupled installation positions, as well as the pylon. Goulos et al. [12] identified a fundamental aerodynamic interference mechanism between the engine, the pylon, and the airframe. It was shown that an aerodynamic interference arises between the fuselage, wing, and the engine inboard side [12,26]. This led to increased flow acceleration on the engine inboard side due to the effective flow area restriction. This resulted in reduced static pressure on the nacelle, exhaust after-body, and pylon compared to the outboard side flow topology. Furthermore, it was noted that due to the wing sweep angle, the engine geometry was axially more overlapped with the wing on the inboard side compared to the outboard side. This amplified the aerodynamic interference effects on the engine inboard side. The combination of these two aerodynamic effects resulted in notable lateral flow asymmetry. Goulos et al. [12] noted that C_d^{Fan} was insensitive to changes in installation position because the fan nozzle was choked. However, a variation range of 5% was found for the unchoked core nozzle C_d^{Core}. Close coupled positions exhibited higher values of C_d^{Core}, compared to forward engine locations.

Rao et al. [13] carried out a RANS CFD campaign to quantify the impact of installation on the exhaust of an aero-engine operating at idle-descent conditions. Rao et al. [13] found that the impact of installed suppression on C_d^{Fan} is approximately 1.6% across the idle-descent phase, relative to an isolated configuration with pylon. This was because the fan nozzle was unchoked throughout the idle descent phase. The impact of installed suppression on C_d^{Core} was found to be more significant. It was shown that the installation effect can lead to an increase of C_d^{Core} of 43% at the top of descent, relative to the isolated configuration. However, at the end of descent, it was shown that the installed suppression effect can reduce C_d^{Core} by roughly 5.4%. This was due to a combination of parameters such as wing loading, fan nozzle pressure ratio (FNPR), and core nozzle pressure ratio (CNPR) which affected the core nozzle base pressure.

1.4 Scope of Present Work. The existing literature is predominantly focused on midcruise conditions [12,23,24,26], with the exception of the work of Rao et al. [13], which tackled the idle-descent phase. With regard to wind-milling conditions, recent studies focused on nacelle drag [16], internal drag [9], and fan stage aerodynamics [27–30]. To the authors' knowledge there are currently no published works that quantify the impact of the installed suppression effect on exhaust performance at wind-milling. However, there is a need to understand this aspect since

the impact of installed suppression on C_d^{Fan} can influence the engine mass flow and the associated nacelle drag [7,8,16].

This work conducted a RANS CFD investigation to quantify the impact of installed suppression on the aerodynamic performance of a civil high by-pass ratio aero-engine exhaust at wind-milling. Analyses were based on the DSJP test rig, which will be tested in the TWT [31] located at the ARA in the UK. The DSJP rig was designed to measure the effect of the installed pressure field on the aerodynamic performance of a civil large separate-jet exhaust. The rig incorporates the DSFRN [21,32], installed under a swept wing designed to replicate the lift-distribution of the NASA CRM wing [25]. RANS CFD simulations were carried out using ANSYS FLUENT [33] for "engine-out" wind-milling scenarios at EOR takeoff, diversion, and cruise conditions. Analyses were performed both with and without the wing to isolate the installed suppression effect on C_d^{Fan} and C_d^{Core}. The effect of FNPR and CNPR, as well as freestream Mach number and high-lift surfaces on the installed suppression effect was quantified.

To the authors' knowledge, this is the first investigation to quantify the installed suppression effect on exhaust performance for wind-milling. The results can be used to inform zero-dimensional (0D) engine performance models and improve predictions of ingested inlet mass flow, which can lead to more accurate predictions of nacelle drag for wind-milling [16]. The results have been used to inform the design and setup of the experimental activity which is planned for 2023.

2 Methodology

2.1 Aircraft Research Association Dual Stream Jet Propulsion Rig. The RANS CFD investigations were based on the DSJP rig (Fig. 1), which will be tested at the ARA TWT [31] in 2023. The DSJP rig was designed to measure the installed suppression effect on the aerodynamic performance of a civil large aero-engine exhaust. The rig incorporates the DSFRN [21,32], installed under a swept wing, which was designed to emulate the lift-distribution of the NASA CRM wing [25].

Analyses were performed for both isolated (Fig. 1(a)) and installed configurations (Figs. 1(b) and 1(c)) to quantify the impact of the wing on C_d^{Fan} and C_d^{Core}. The impact of FNPR and CNPR, as well as freestream M_∞ and high-lift surfaces, on the installed suppression effect was also evaluated. To understand the impact of the high-lift surfaces, analyses were carried out using two different wing configurations provided by ARA: (1) 0 degree flap wing (Fig. 1(b)) and (2) 20 degree flap wing (Fig. 1(c)). The former configuration is representative of a clean-wing deployed during diversion and cruise. The latter configuration employs a 20-degree trailing edge flap that represents the high-lift surfaces and is consistent with EOR conditions. The aim of this work is to carry out the necessary numerical analyses to support the experimental activity that will take place in 2023. This activity will use the geometries described in this paper (Fig. 1) to quantify experimentally the installed suppression effect on exhaust performance at wind-milling conditions.

2.2 Computational Fluid Dynamics Approach. The ARA TWT is an atmospheric wind-tunnel that employs porous walls of the working section [31]. In this work, it was decided to avoid the complexity associated with modeling the effects of wall porosity. Instead, a far-field type boundary condition (BC) was used. This was done by using a hemispherical domain with diameter equal to $100 \times C_{\text{ref}}$, where C_{ref} is the reference DSJP wing chord length (Fig. 2). The freestream flow conditions were modeled using a pressure far-field BC with prescribed p_∞, M_∞, and T_∞. The fan and core nozzle inlet boundaries were modeled as pressure inlet BCs with defined P_0 and T_0. All surfaces were modeled as adiabatic and viscous no-slip walls, with the exception of the ground plane which was modeled as a slip wall.

A hybrid meshing methodology was used for the isolated and installed DSJP configurations (Fig. 3) [34]. Structured prism layers were used near the viscous walls with $y^+ < 1$ for all wall-adjacent nodes. Unstructured tetrahedral elements were used to populate the
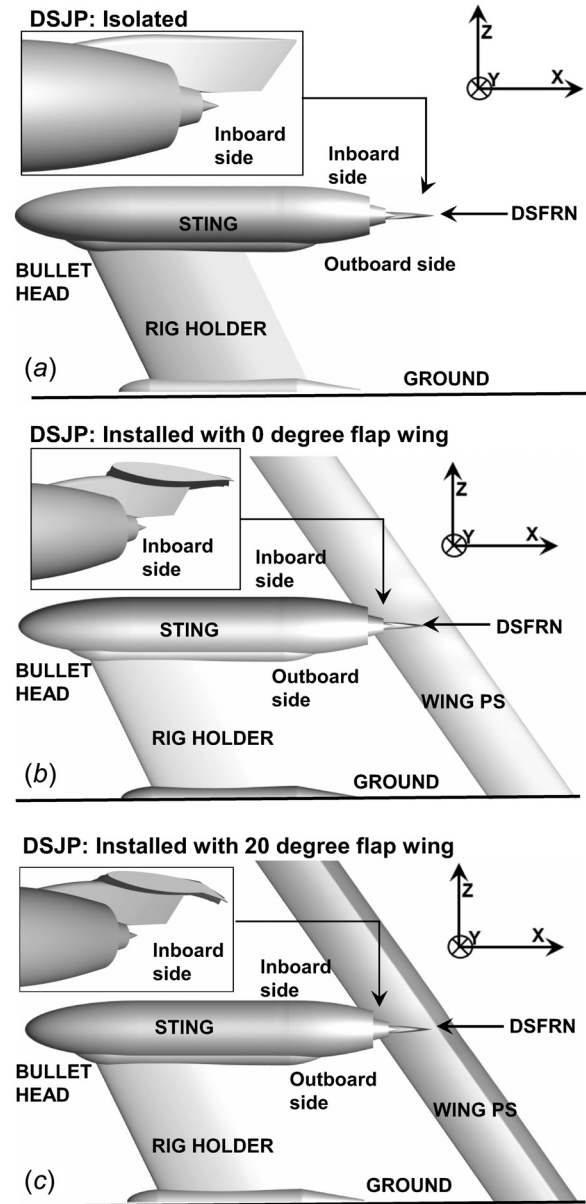

Fig. 1 ARA DSJP rig illustration: (a) isolated configuration (wing-off), (b) installed configuration with 0 degree flap wing (clean wing-on), and (c) installed configuration with 20 degree flap wing (20 degree flap wing-on)
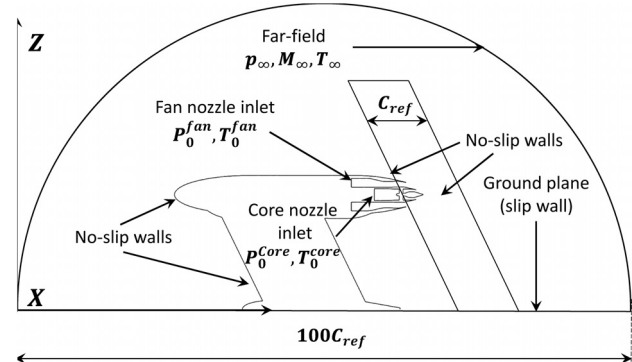

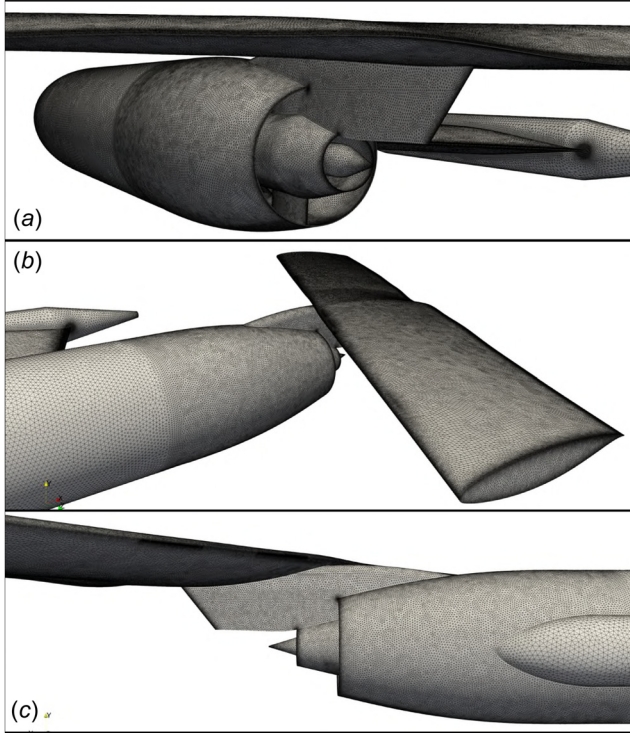**Fig. 2 Computational domain and boundary condition**

Fig. 3 Surface mesh close-up on DSJP rig (0 degree flap wing): (a) exhaust and pylon, (b) sting and wing, and (c) exhaust outboard side

remainder of the computational domain. Near-wall unstructured mesh refinement was performed based on local wall-curvature and surface-proximity arguments [34]. Unstructured mesh refinement zones were defined near the vicinity of the exhaust, pylon, and wing to resolve localized flow features. The spatial discretization was based on the grid verification activities. These showed that the hybrid meshes required approximately 50×10^6 and 100×10^6 elements for the isolated and installed cases, respectively. Specifically, for the installed configuration (Fig. 1(b)), the differences in C_d^{Fan} and C_d^{Core} were 0.03% and 0.08% at DP ($M_\infty = 0.85$, FNPR = 2.4, and CNPR = 2.0), respectively, between meshes with 100×10^6 and 200×10^6 elements.

The simulations used an implicit, density-based, and compressible Favre-averaged CFD approach [35] coupled with the $k - \omega$ shear-stress transport turbulence model [36]. The flow-field gradients were calculated based on the Green–Gauss node based method. A second-order accurate upwind scheme was used for the spatial discretization of primitive variables, turbulent kinetic energy k, and specific dissipation rate ω. Kinetic theory was used to calculate thermal conductivity κ [35]. The method accounted for variable gas properties based an 8th order piecewise polynomial expression for the calculation of specific heat capacity as a function of static temperature [11]. Dynamic viscosity was calculated using Sutherland's law [37].

The RANS CFD approach was validated by Goulos et al. [12] based on experimental data published by Mikkelsen et al. [32] for the DSFRN. Simulations were carried out for an FNPR range $\left(\mathrm{FNPR} = \frac{P_0^{\mathrm{Fan}}}{p_\infty}\right)$ between 1.4 and 2.8 and for ground-level static conditions ($M_\infty \approx 0$). This was carried out using a fixed Extraction Ratio of $\left(\mathrm{ER} = \frac{\mathrm{FNPR}}{\mathrm{CNPR}} = 1.2\right)$, where $\mathrm{CNPR} = \frac{P_0^{\mathrm{Core}}}{p_\infty}$. Goulos et al. [12] found that the Root Mean Square (RMS) difference between CFD predictions and measured data, was approximately 0.04%, 0.30%, and 0.42% for C_v, C_d^{Fan}, and C_d^{Core}, respectively.

2.3 Exhaust System Performance Accounting. The definitions of C_d^{Fan} and C_d^{Core} for the DSFRN wind-tunnel tests were

provided by Mikkelsen et al. [32]. These nondimensional coefficients were defined in a way to allow direct comparisons with experimental and computational results. These definitions are also used in this work to establish consistency with the standard accounting of Mikkelsen et al. [32].

The discharge coefficient for a nozzle is defined as the ratio of the actual nozzle mass flow over the ideal nozzle mass flow ($\dot{m}_{\mathrm{Ideal}}$) resulting from isentropic expansion to ambient static pressure. The ideal nozzle mass flow (Eq. (1)) for prescribed values of inlet total pressure P_0 and total temperature T_0, can be calculated as follows:

$$\dot{m}_{\mathrm{Ideal}} = A_{\mathrm{throat}} P_0 \left(\frac{1}{\lambda}\right)^{\frac{1}{\gamma}} \sqrt{\frac{2\gamma}{(\gamma - 1)RT_0}\left(1 - \left(\frac{1}{\lambda}\right)^{\frac{\gamma-1}{\gamma}}\right)} \quad (1)$$

where A_{throat} is the nozzle throat area, $\lambda = \frac{P_0}{P_{\mathrm{amb}}}$, p_∞ denotes the ambient static pressure, R is the gas constant for air, and γ is the ratio of specific heats. It is noted that for $\lambda \geq \lambda_{\mathrm{crit}} = \left(\frac{\gamma+1}{2}\right)^{\frac{\gamma}{\gamma-1}}$, the value of λ_{crit} is used in Eq. (1) instead of λ.

Based on the definition of ideal mass flow (Eq. (1)), the fan and core nozzle discharge coefficients can be written as follows:

$$C_d^{\mathrm{Fan}} = \frac{\dot{m}_{\mathrm{CFD}}^{\mathrm{Fan}}}{\dot{m}_{\mathrm{Ideal}}^{\mathrm{Fan}}} \quad C_d^{\mathrm{Core}} = \frac{\dot{m}_{\mathrm{CFD}}^{\mathrm{Core}}}{\dot{m}_{\mathrm{Ideal}}^{\mathrm{Core}}} \quad (2)$$

The values of $\dot{m}_{\mathrm{CFD}}$ in Eq. (2) for the fan and core nozzles are obtained by integrating the axial mass fluxes ($\rho \times V_x$) across the nozzle entry planes, where ρ is the density and V_x is the axial velocity.

3 Results and Discussion

3.1 Exhaust Inlet Conditions at Wind-Milling. This section outlines the derivation of representative FNPR and CNPR ranges that were used for exhaust aerodynamic analysis at wind-milling. 0D calculations were carried out based on prescribed fan stage loss coefficients [9] applied to the fan inlet dynamic head q^{Fan}. Analyses were carried out for three (3) operating points: (a) EOR at $M_\infty = 0.25$, (b) diversion at $M_\infty = 0.65$, and cruise at $M_\infty = 0.85$. The fan inlet total pressure was calculated on the basis of ram pressure rise $\left(\frac{P_0}{p_\infty}\right)^{\mathrm{Ram}}$ assuming isentropic flow through the intake. This ram pressure rise represents the highest possible values of FNPR and CNPR which would occur under isentropic flow conditions. Fan stage total pressure loss coefficients within a range of $10\% < \frac{\Delta P_0^{\mathrm{Fan}}}{q^{\mathrm{Fan}}} < 100\%$ were applied on $\left(\frac{P_0}{p_\infty}\right)^{\mathrm{Ram}}$ for each M_∞ to quantify the variation range of wind-milling FNPR (Table 1).

Table 1 shows that for the WM EOR condition ($M_\infty = 0.25$), FNPR can vary between ≈ 1.04 (isentropic flow) to ≈ 1.0 for $\frac{\Delta P_0^{\mathrm{Fan}}}{q^{\mathrm{Fan}}} = 50\%$, which is a limiting case since FNPR reduces below 1.0 for $\frac{\Delta P_0^{\mathrm{Fan}}}{q^{\mathrm{Fan}}} > 50\%$. Similar observations can be made for the diversion ($M_\infty = 0.65$) and cruise cases ($M_\infty = 0.85$).

The WM FNPR ranges showed in Table 1 were derived for a wide range of fan stage total pressure loss coefficients $\frac{\Delta P_0^{\mathrm{Fan}}}{q^{\mathrm{Fan}}}$. Nominal WM

Table 1 Impact of fan stage total pressure loss coefficient on FNPR at Wind-Milling (WM) conditions

Condition	M_∞	$\left(\frac{P_0}{p_\infty}\right)^{\mathrm{Ram}}$	FNPR	FNPR	FNPR
$\frac{\Delta P_0^{\mathrm{Fan}}}{q^{\mathrm{Fan}}}$	—	0%	10%	50%	100%
WM (EOR)	0.25	1.04	1.03	≈ 1.0	<1
WM (Div.)	0.65	1.33	1.30	1.24	1.13
WM (Cruise)	0.85	1.60	1.58	1.49	1.38

FNPR values were subsequently defined by fixing $\frac{\Delta P_0^{\text{Fan}}}{q^{\text{Fan}}}$ for each M_∞ to define representative wind-milling points. Zachos [9] showed that $\frac{\Delta P_0^{\text{Fan}}}{q^{\text{Fan}}}$ rises notably with M_∞. For the WM EOR condition ($M_\infty = 0.25$), $\frac{\Delta P_0^{\text{Fan}}}{q^{\text{Fan}}}$ is closer to 10%, giving a nominal WM FNPR of 1.03. For WM diversion ($M_\infty = 0.65$) and WM cruise ($M_\infty = 0.85$), $\frac{\Delta P_0^{\text{Fan}}}{q^{\text{Fan}}}$ is closer to 50% and 100%, respectively [9]. This yielded nominal WM FNPR values of 1.24 and 1.38 for diversion and cruise, respectively.

The core nozzle operates consistently at notably lower pressure ratios compared to the fan nozzle during wind-milling [9]. This is due to the higher total pressure losses through the engine core, relative to the LP system [9]. Within this work, CFD analyses were carried out down to the lowest feasible values of CNPR before total flow-reversal would appear on the core nozzle inlet boundary (Fig. 1). This process allowed to identify the limiting cases in terms of low CNPR as well as quantify the impact of CNPR on the installed suppression effect.

The estimates obtained in this section were only used to establish representative ranges of FNPR and CNPR at wind-milling. It is acknowledged that the true values of wind-milling FNPR and CNPR will depend on many parameters such as fan stage loss, engine core loss, exhaust performance, and installation. Within this work it was decided to assess the behavior of the exhaust system across the established FNPR and CNPR ranges (Table 1) to understand the sensitivity of the installed suppression effect around the nominal wind-milling points.

3.2 Installed Suppression Effect at Wind-Milling End of Runway Conditions.
RANS CFD simulations were initially performed for the wind-milling EOR condition with $M_\infty = 0.25$. Analyses were carried out for a FNPR range of $1.01 < \text{FNPR} < 1.05$. The associated CNPR range was $1.01 < \text{CNPR} < 1.03$. A minimum value of 1.01 was set for both FNPR and CNPR to ensure positive mass flow through the fan and core nozzles. These ranges were selected to quantify the sensitivity of the installed suppression effect around the nominal wind-milling point (FNPR = 1.03).

Figure 4 presents the installed fan nozzle suppression effect in terms of $(C_{d,\text{Installed}}^{\text{Fan}} - C_{d,\text{Isolated}}^{\text{Fan}})(\%)$ as a function of FNPR for $M_\infty = 0.25$. Results are presented for the 0-degree flap wing, as well as the 20-degree flap wing. The effect of installed suppression increases considerably with reducing FNPR. For the 20-degree flap wing, the impact of installed suppression is -39% for FNPR = 1.01 and -6% for FNPR = 1.05. This indicates the strong dependency of the installed suppression effect on FNPR for this low FNPR range. The installed suppression effect reduces considerably for the 0 degree flap wing relative to the 20 degree flap arrangement. For example, the installed suppression effect on C_d^{Fan} for FNPR = 1.01 is reduced to -15%. The installed suppression effect reduces to -2.5% when FNPR is increased to 1.05. This highlights the strong

impact of the high-lift surface on C_d^{Fan} suppression which is about -24% for FNPR = 1.01. However, the impact of the high-lift surface on the installed suppression reduces to approximately -2.5% for FNPR = 1.05.

Figure 5 presents the installed core nozzle suppression effect in terms of $(C_{d,\text{Installed}}^{\text{Core}} - C_{d,\text{Isolated}}^{\text{Core}})(\%)$ as a function of CNPR and FNPR for $M_\infty = 0.25$. Results are presented for the 0-degree flap wing, as well as the 20-degree flap wing. The installed suppression effect is strongly dependent on CNPR. For FNPR = 1.03 and for the 20-degree flap wing, the installed suppression effect on C_d^{Core} is roughly -51% when CNPR = 1.01. This reduces to -9% when CNPR = 1.03. The effect of FNPR on the installed suppression effect is also evident. For CNPR = 1.01 and for the 20 degree flap wing, the installed suppression effect on C_d^{Core} reduces from -51% when FNPR = 1.03, to -39% when FNPR = 1.01. The impact of the high-lift surfaces is also strongly dependent on CNPR. For CNPR = 1.01 and FNPR = 1.03, the difference in the installed suppression effect on C_d^{Core} between the 20 degree and 0 degree configurations, is -39%. However, the impact of the high-lift surface on the installed suppression effect reduces to -6% for CNPR = 1.03.

Figure 6 illustrates the aerodynamic behavior of the exhaust system for EOR wind-milling condition at $M_\infty = 0.25$, FNPR = 1.03, and CNPR = 1.03. Flow-field visualizations are presented along the meridional exhaust plane as viewed from the engine inboard side (Fig. 1). Static pressure is shown on the exhaust and pylon walls, while Mach number is plotted on the fluid domain. Results are presented for the isolated exhaust (Fig. 6(a)), as well as for the installed configurations with 0-degree (Fig. 6(b)) and 20-degree wing flap angles (Fig. 6(c)).

Figure 6 shows that the aerodynamic effect of the wing (Figs. 6(b) and 6(c)) is to increase the mean freestream flow deflection angle relative to the isolated configuration (Fig. 6(a)). This freestream flow deflection is more potent for the 20-degree flap wing (Fig. 6(c)) relative to the 0-degree flap configuration (Fig. 6(b)), as expected. For the 0-degree flap wing angle, Fig. 6(b) shows that the installed pressure field results in an increase of static pressure of approximately 0.5 kPa on the fan nozzle top-line and core plug, relative to the isolated configuration (Fig. 6(a)). For the 20 degree flap wing (Fig. 6(c)), the further increase in flow deflection results in a further increase of static pressure of approximately 0.5 kPa on the nacelle, exhaust, and pylon surfaces, relative to the 0-degree flap wing (Fig. 6(b)). These increases in static pressure for the installed cases result in the pressurization of the fan and core nozzle base surfaces, which lead to the installed suppression effect on both C_d^{Fan} and C_d^{Core}, as previously quantified in Figs. 4 and 5.

The DSFRN exhaust has convergent fan and core nozzles [32]. Therefore the fan and core nozzle exit planes are aligned axially with the nozzle throat. As a result, the mass flux distribution at the fan and core nozzle exit can be used to identify the key aerodynamic mechanisms with which the installed suppression effect influences C_d^{Fan} and C_d^{Core}. Figure 7 presents the normalized mass flux
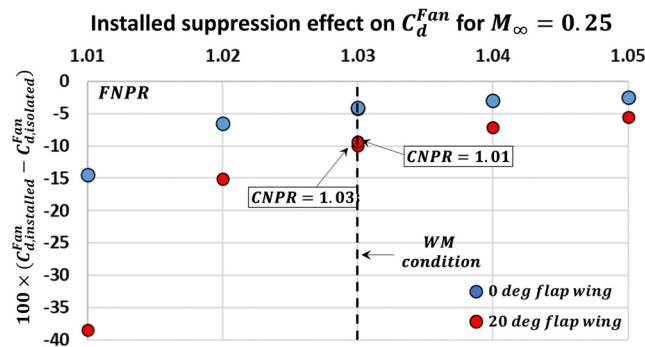

Fig. 4 Impact of FNPR on installed fan nozzle suppression effect $(C_{d,\text{Installed}}^{\text{Fan}} - C_{d,\text{Isolated}}^{\text{Fan}})(\%)$ for WM EOR conditions: $M_\infty = 0.25$
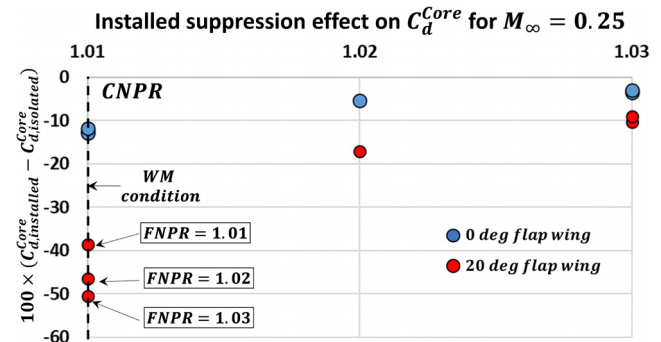

Fig. 5 Impact of CNPR and FNPR on installed core nozzle suppression effect $(C_{d,\text{Installed}}^{\text{Core}} - C_{d,\text{Isolated}}^{\text{Core}})(\%)$ for WM EOR conditions: $M_\infty = 0.25$
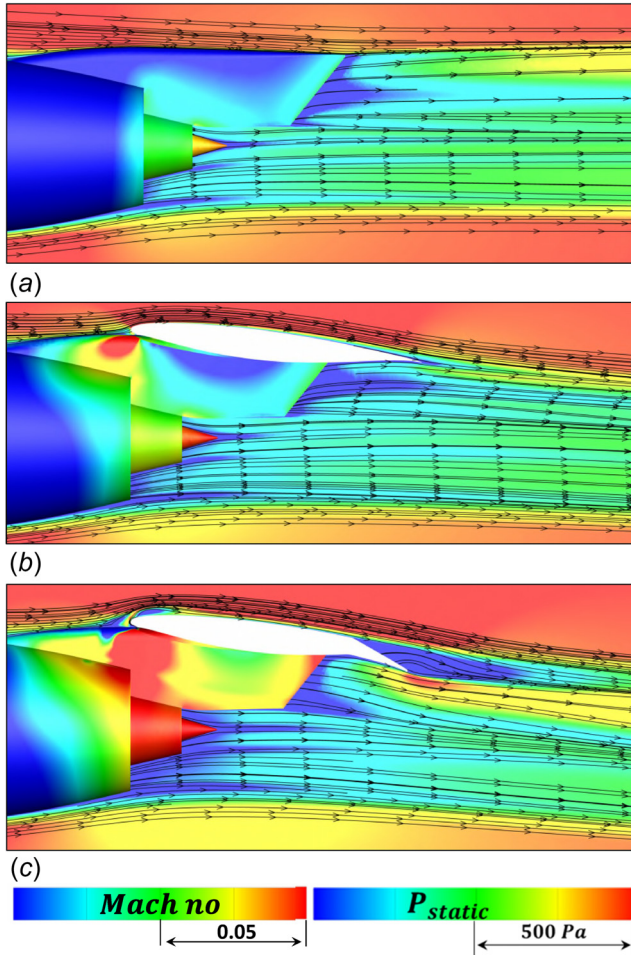
Fig. 6 DSJP rig wind-milling exhaust aerodynamics at inboard side: surface static pressure and flow-field Mach number distribution for $M_\infty = 0.25$, FNPR = 1.03 and CNPR = 1.03: (*a*) isolated, (*b*) installed with 0 degree flap wing, and (*c*) installed with 20 degree flap wing

distribution at the fan nozzle exit (throat) plane which is defined as follows:

$$\overline{\dot{m}}_{\text{Throat}}^{\text{Fan}} = \frac{(\rho V_x)_{\text{Throat}}^{\text{Fan}}}{\left(\dot{m}_{\text{CFD}}^{\text{Fan}} / A_{\text{throat}}^{\text{Fan}}\right)_{\text{Isolated}}} \qquad (3)$$

where normalization takes place with the average fan nozzle throat mass flux of the isolated configuration $(\dot{m}_{\text{CFD}}^{\text{Fan}} / A_{\text{throat}}^{\text{Fan}})_{\text{Isolated}}$. Results are presented for the isolated (Fig. 7(*a*)) and the installed configurations with the 0-degree (Fig. 7(*b*)) and 20-degree flap wings (Fig. 7(*c*)).

The impact of the installed suppression for the 0-degree flap wing (Fig. 7(*b*)), manifests predominantly through a mass flux reduction on the fan nozzle exit outboard side. This reduction in $\overline{\dot{m}}_{\text{Throat}}^{\text{Fan}}$ is of the order of 10%, relative to the isolated case (Fig. 7(*a*)). This is due to the closer proximity of the wing Leading Edge (LE) stagnation point to the fan nozzle exit on the outboard side, relative to the inboard side due to the wing sweep angle (Fig. 1). The high static pressure due to the wing propagates to pressurize the fan nozzle base on the outboard side top-line. This reduces the mass flux on the outboard side and decreases the installed C_d^{Fan} by almost 4% relative to the isolated case (Fig. 4).

The polarity of the mass flux reduction due to the installed suppression effect appears to reverse for the 20-degree flap wing (Fig. 7(*c*)). For this arrangement, the installed suppression effect manifests primarily through a mass flux decrease on the fan nozzle
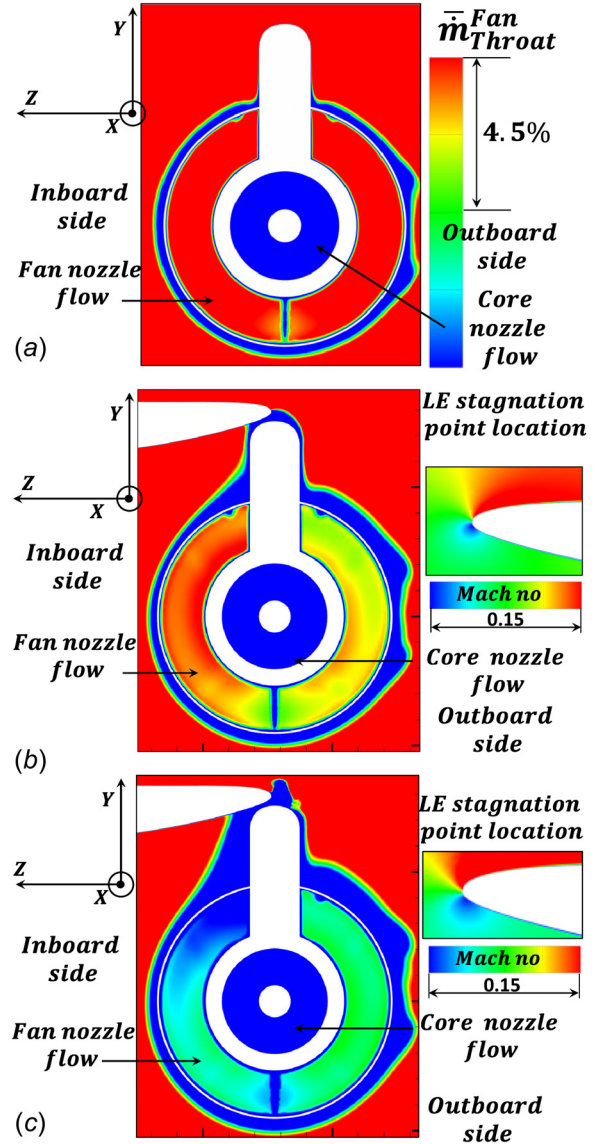

Fig. 7 Normalized mass flux distribution at the fan nozzle exit plane for $M_\infty = 0.25$, FNPR = 1.03 and CNPR = 1.03: (*a*) isolated, (*b*) installed with 0 degree flap wing, and (*c*) installed with 20 degree flap wing

exit inboard side near the top-line. The observed reduction in $\overline{\dot{m}}_{\text{Throat}}^{\text{Fan}}$ is almost 15%, relative to the isolated configuration (Fig. 7(*a*)). This suggests that for the 20-degree flap wing, the installed suppression mechanism is different compared to the clean wing case (Fig. 7(*b*)). The dominant suppression mechanism for the 20-degree flap wing arrangement is due to the static pressure rise on the wing Pressure Side (PS) due to the presence of the flap (Fig. 6(*c*)). This static pressure rise propagates upstream to pressurize the fan nozzle base. However, the wing Trailing Edge (TE) flap is closer to the fan nozzle exit on the inboard side, compared to the outboard side. This is again due to the swept wing arrangement (Figs. 1(*b*) and 1(*c*)). Therefore, the associated fan nozzle base pressurization is more potent on the inboard side compared to the outboard side, leading to a higher mass flux reduction. This results in a C_d^{Fan} decrease of approximately 10% relative to the isolated configuration (Fig. 4).

Figure 8 presents the normalized mass flux distribution at the core nozzle exit (throat) plane, which is defined as follows:

$$\overline{\dot{m}}_{\text{Throat}}^{\text{Core}} = \frac{(\rho V_x)_{\text{Throat}}^{\text{Core}}}{\left(\dot{m}_{\text{CFD}}^{\text{Core}} / A_{\text{throat}}^{\text{Core}}\right)_{\text{Isolated}}} \qquad (4)$$
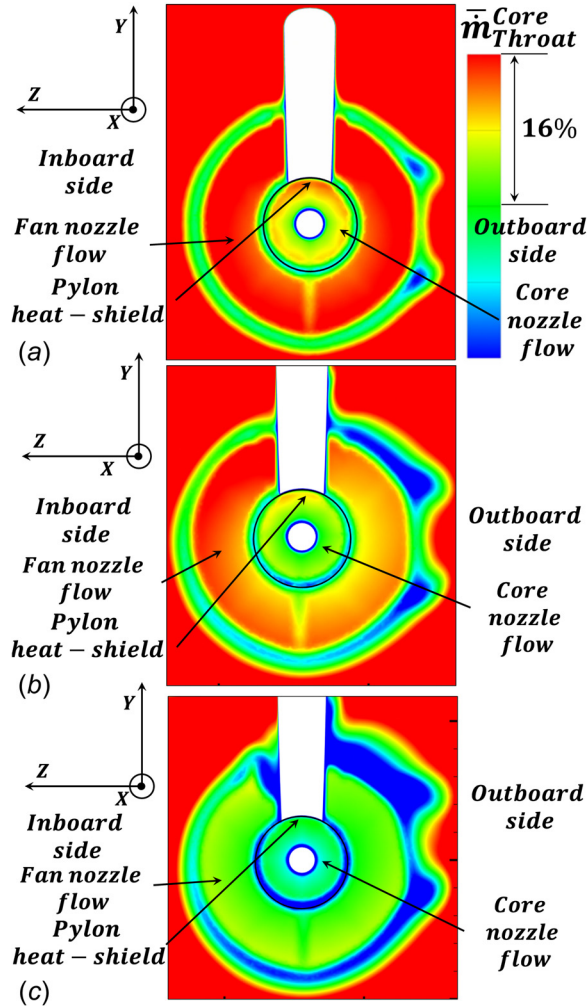
Fig. 8 Normalized mass flux distribution at the core nozzle exit plane for $M_\infty = 0.25$, FNPR = 1.03 and CNPR = 1.03: (a) isolated, (b) installed with 0 degree flap wing, and (c) installed with 20 degree flap wing

where normalization is carried out with the average core nozzle throat mass flux of the isolated configuration $(\dot{m}_{\text{CFD}}^{\text{Core}}/A_{\text{throat}}^{\text{Fan}})_{\text{Isolated}}$. Results are presented for the isolated (Fig. 8(a)) and the installed configurations with the 0-degree flap (Fig. 8(b)) and 20 degree flap wings (Fig. 8(c)).

Figure 8(a) shows that for the isolated exhaust configuration the mass flux is increased under the pylon and near the vicinity of the core after-body trailing edge top-line. The effect of the pylon is to shield the core nozzle exit flow from the "freestream" and "fan" suppression effects [21,22] and therefore to increase the mass flux locally. This pylon effect on the core nozzle exit flow was also noted by Rao et al. [13] for idle-descent conditions. For the 0-degree flap wing case (Fig. 8(b)), the installed suppression effect on the core nozzle exit flow manifests in a uniform manner without clear biasing toward the inboard or outboard side. However, there is a vertical biasing toward the position underneath the pylon heat-shield. Specifically, the observed reduction in $\overline{\dot{m}}_{\text{Throat}}^{\text{Core}}$ underneath the pylon heat-shield is approximately 10%, relative to the isolated case (Fig. 8(a)). This effect decreases the overall installed C_d^{Core} by almost 2.5% relative to the isolated configuration (Fig. 5).

The character of the installed suppression effect on the core nozzle exit mass flux for the 20-degree flap wing (Fig. 8(c)) is similar to that discussed for the 0-degree flap wing arrangement. However, the installed suppression effect is more potent compared to the 0-degree case. The associated $\overline{\dot{m}}_{\text{Throat}}^{\text{Core}}$ reduction under the pylon heat-

shield is approximately 20%, relative to the isolated case (Fig. 8(a)). As a result, the pylon shielding effect noted for the isolated arrangement (Fig. 8(a)) has been almost completely eroded for the 20-degree case (Fig. 8(c)). This results in a reduction of installed C_d^{Core} by approximately 10.0% relative to the isolated configuration (Fig. 5).
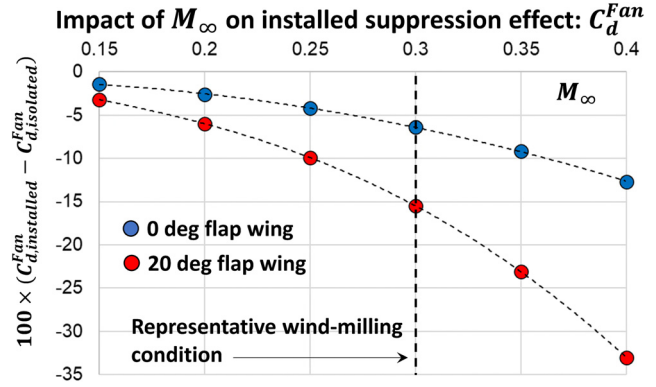
3.3 Impact of Free-Stream Mach Number. A numerical investigation was carried out to understand the impact of M_∞ on the installed suppression effect for C_d^{Fan} and C_d^{Core} (Figs. 9 and 10, respectively). All analyses were carried out for FNPR = 1.03 and CNPR = 1.03. Figure 9 shows that M_∞ has a significant impact of the installed C_d^{Fan} suppression effect. For the 20-degree flap wing, the installed suppression effect on C_d^{Fan} for $M_\infty = 0.15$ is approximately -3.5%. However, this increases to roughly -16% for a representative wind-milling condition of $M_\infty = 0.30$. This is due to the increased wing lift at higher freestream Mach numbers, leading to an increase the local wing static pressure which propagates on the exhaust and pylon surfaces, and suppresses the fan nozzle mass flow. Furthermore, it can be observed that the potency of the M_∞ effect on the installed fan nozzle suppression is dependent on the wing configuration. The difference in the installed fan nozzle suppression effect between the 20-degree and 0-degree flap wings is approximately -2% for $M_\infty = 0.15$. However, this difference increases to -10% for $M_\infty = 0.30$. This is due to higher circulation of the 20-degree flap wing and the aerodynamic mechanisms exposed in Figs. 6 and 7. For $M_\infty = 0.4$, the installed suppression effect on C_d^{Fan} can reach up to -12.5% and -33.1% for the 0-degree and 20-degree flap wings, respectively. However,
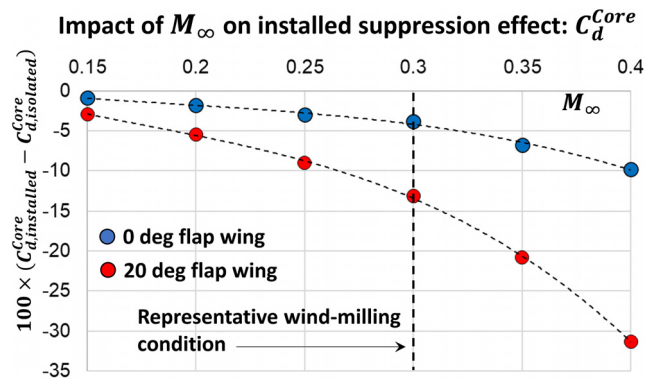

Fig. 9 Impact of M_∞ on installed fan nozzle suppression effect $(C_{d,\text{Installed}}^{\text{Fan}} - C_{d,\text{Isolated}}^{\text{Fan}})(\%)$ for WM EOR conditions: FNPR = 1.03 and CNPR = 1.03

Fig. 10 Impact of M_∞ on installed core nozzle suppression effect $(C_{d,\text{Installed}}^{\text{Core}} - C_{d,\text{Isolated}}^{\text{Core}})(\%)$ for WM EOR conditions: FNPR = 1.03 and CNPR = 1.03

Fig. 11 Impact of FNPR and installation on C_d^{Fan} for WM diversion conditions: $M_\infty = 0.65$
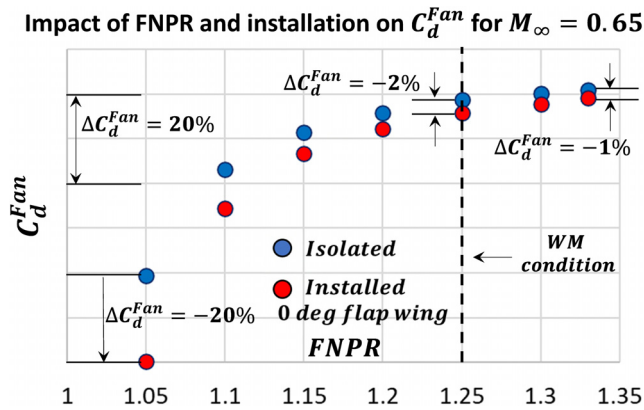

Fig. 13 Impact of FNPR and installation on C_d^{Fan} around WM cruise conditions: $M_\infty = 0.85$

during flight the high-lift surfaces would most likely be retracted for $M_\infty \geq 0.4$. It is, therefore, unlikely that the fan nozzle would operate with an installed suppression effect of -35.5% in flight. Therefore, it can be concluded that for a representative WM EOR scenario with $M_\infty = 0.30$, the installed suppression effect on C_d^{Fan} can reach up to -16% for FNPR = 1.03.

Figure 10 shows that the installed suppression effect for the core nozzle follows a similar behavior to that of the fan nozzle (Fig. 9). For the 20 degree flap wing, the installed suppression effect on C_d^{Core} for $M_\infty = 0.15$ is nearly -3%, and this increases to roughly -13% for $M_\infty = 0.30$. The impact of the wing configuration is similar to that observed for C_d^{Fan} (Fig. 9). For $M_\infty = 0.4$ the installed suppression effect on C_d^{Core} can reach approximately -10% and -31% for the 0 degree and 20 degree flap wings, respectively. However, since the high-lift surfaces would most likely be retracted for $M_\infty = 0.4$, it is unlikely that the core nozzle would operate with such a high installed suppression effect (-32%) in flight. The aerodynamic mechanisms that govern the behavior of the installed C_d^{Core} are similar to those discussed for C_d^{Fan} (Figs. 6 and 8).

3.4 Installed Suppression at Wind-Milling Diversion Conditions. Figure 11 illustrates the impact of FNPR and installed suppression effect on C_d^{Fan} for wind-milling diversion conditions at $M_\infty = 0.65$. Analyses were carried out for a FNPR range of $1.05 <$ FNPR < 1.33 to quantify the sensitivity of the installed suppression around the nominal wind-milling point (FNPR ≈ 1.25). The installed analysis has been carried out using the 0 degree flap wing only. The corresponding wind-milling condition in terms of FNPR is also outlined in Fig. 11 for consistency. It can be observed that the installed suppression effect is highly dependent on FNPR. For
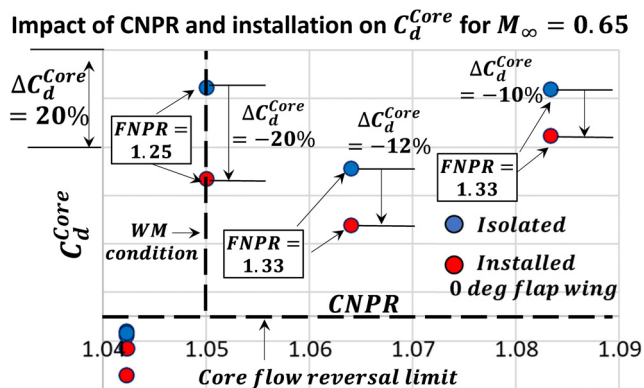
FNPR = 1.05, the installed C_d^{Fan} suppression effect ($C_{d,\text{Installed}}^{\text{Fan}} - C_{d,\text{Isolated}}^{\text{Fan}}$) is of the order of -20%. However, this reduces to approximately -2% for the nominal wind-milling condition at FNPR ≈ 1.25 (Table 1). The installed C_d^{Fan} suppression effect is further reduced to approximately -1% for FNPR = 1.33. This is due to the increased robustness of the fan nozzle flow at higher FNPR that renders it less sensitive to external flow static pressure disturbances, relative to the low FNPR conditions. The aerodynamic mechanisms that govern the behavior of the installed suppression effect on C_d^{Fan} are similar to those discussed for the WM EOR condition for the 0 degree flap wing.

The impact of CNPR and FNPR on C_d^{Core} for wind-milling diversion conditions at $M_\infty = 0.65$ is presented in Fig. 12. Results are presented for the isolated and installed configurations with the 0-degree flap wing. It is once again observed that C_d^{Core} is strongly dependent on CNPR. For the nominal wind-milling condition (CNPR ≈ 1.05), the magnitude of the installed suppression effect ($C_{d,\text{Installed}}^{\text{Core}} - C_{d,\text{Isolated}}^{\text{Core}}$) is nearly -20%. This reduces to approximately -10% for CNPR ≈ 1.084. This is due to the same aerodynamic reasons discussed for the WM EOR condition. The impact of FNPR on the absolute values of installed and isolated C_d^{Core} is also evident. For the nominal wind-milling condition (CNPR ≈ 1.05), the FNPR is approximately 1.25 (Table 1). The FNPR is increased to 1.33 for higher values of CNPR (CNPR > 1.06). This increase in FNPR reduces C_d^{Core} by approximately 10% when moving from CNPR ≈ 1.05 to CNPR ≈ 1.064 and above. Furthermore, the analysis also revealed a limiting case of CNPR < 1.05 for which the results show that there will be a "no flow" condition. This was observed for both installed and isolated cases and is due the low value of core nozzle inlet P_0, which is unable to overcome the freestream, fan, and installed suppression effects.

Fig. 12 Impact of CNPR and installation on C_d^{Core} for WM diversion conditions: $M_\infty = 0.65$

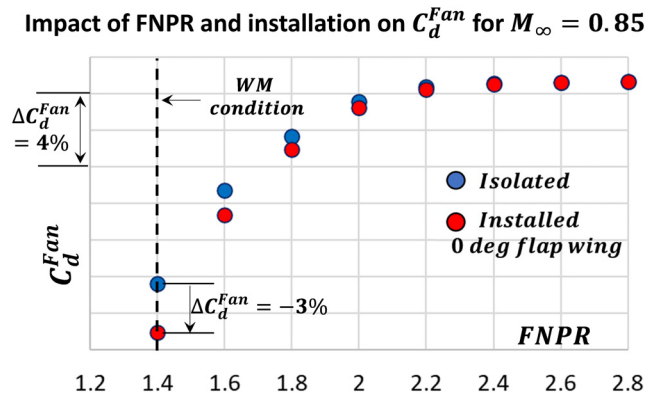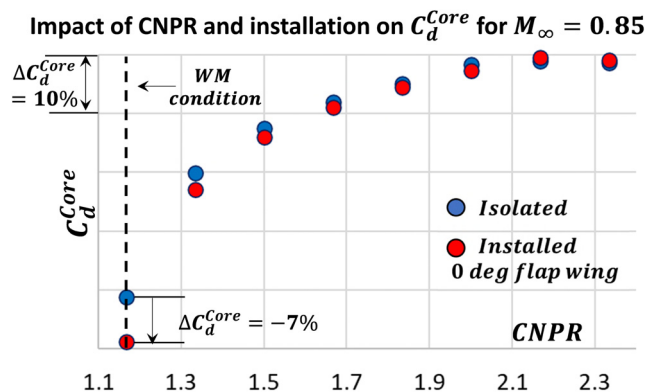**Fig. 14 Impact of CNPR and installation on C_d^{Core} around WM cruise conditions: $M_\infty = 0.85$**

3.5 Installed Suppression at Wind-Milling Cruise Conditions. Figures 13 and 14 illustrate the impact of installation on C_d^{Fan} and C_d^{Core} at cruise conditions with $M_\infty = 0.85$. The installed analyses have been carried out using the 0 degree flap wing only since the high-lift surfaces are not deployed for this condition. Simulation is carried for $1.4 < \text{FNPR} < 2.8$ with a fixed value of Extraction Ratio (ER = FNPR/CNPR = 1.2).

Figure 13 presents the impact of FNPR on the installed and isolated C_d^{Fan}. The nominal wind-milling condition (FNPR ≈ 1.4) is also annotated (Table 1). It can be noted that the installed suppression effect ($C_{d,\text{Installed}}^{\text{Fan}} - C_{d,\text{Isolated}}^{\text{Fan}}$) is almost -3% for the nominal wind-milling condition at FNPR ≈ 1.4. However, the installed suppression effect on C_d^{Fan} effectively becomes zero for FNPR > 2.0. This is due the chocking of the fan nozzle, which renders it insensitive to external static pressure disturbances [12].

A similar behavior is observed for C_d^{Core} in Fig. 14. The impact of installed suppression on the core nozzle flow ($C_{d,\text{Installed}}^{\text{Core}} - C_{d,\text{Isolated}}^{\text{Core}}$) is approximately -7% when approaching the nominal wind-milling condition for CNPR ≈ 1.1. However, the installed suppression effect disappears for CNPR > 2.0 when the core nozzle chokes and the external static pressure is unable to propagate upstream of the core nozzle throat.

4 Conclusions

This work investigated the effect of wing integration on the aerodynamic behavior of a large civil aero-engine exhaust at wind-milling. The work was based on the DSJP test rig, which will be tested in the TWT located at the ARA in the UK. The DSJP rig was designed to measure the installed suppression effect on the fan and core nozzle discharge coefficients of the Dual Separate Flow Reference Nozzle. A 0D analysis was carried out to establish representative ranges of fan and core nozzle pressure ratios for "engine-out" wind-milling scenarios at EOR takeoff, diversion, and cruise conditions. RANS CFD simulations were done to quantify the impact of the installed suppression on C_d^{Fan} and C_d^{Core} at wind-milling. The impact of fan and core nozzle pressure ratios, as well as freestream Mach number and high-lift surfaces were also quantified. The dominant aerodynamic mechanisms of installed suppression were identified and exposed.

It was shown that for wind-milling EOR conditions at high-lift, the installed pressure field can reduce the fan and core nozzle discharge coefficients by up to 16% and 13%, respectively, relative to the isolated configuration. A lateral biasing of installed flow suppression was found toward the fan cowl inboard side top-line which was attributed to the proximity of the swept wing TE flap to the fan nozzle exit. A vertical biasing of the installed suppression effect was found for the core nozzle flow and the effect was amplified underneath the pylon heat-shield. For wing-milling diversion conditions, the installed suppression effect can reduce the fan and core nozzle discharge coefficients by 2% and 20%, respectively. The high sensitivity of C_d^{Core} to the installed pressure field was due to the very low value of $CNPR$ for this condition, which was close to the core flow reversal limit. For wind-milling cruise conditions, it was shown that the installed suppression effect can reduce the fan and core nozzle discharge coefficients by nearly 3% and 7%.

To the authors' knowledge, this the first investigation to quantify the installed suppression effect on the fan and core nozzle discharge coefficients at wind-milling. The results can be used to inform 0D engine performance models and improve predictions of ingested engine mass flow, which can lead to more accurate predictions of wind-milling nacelle drag. The results have been used to inform the design and setup of the experimental activity which is planned for 2023.

Data Availability Statement

Due to commercial confidentiality agreements the supporting data are not available.

Nomenclature

A = surface area, m^2
BC = boundary condition
C_d = exhaust nozzle discharge coefficient
C_{ref} = reference chord length, m
CFD = referring to CFD flow solutions
Core = referring to the core nozzle
CNPR = core nozzle pressure ratio, $= P_0^{\text{Core}}/p_\infty$
Crit. = referring to critical flow conditions
DP & OD = design-point and off-design, respectively
ER = extraction ratio, FNPR/CNPR
$\dot{m}$ = mass flow rate, kg/sec
Fan = referring to the fan nozzle
FNPR = fan nozzle pressure ratio, $= P_0^{\text{Fan}}/p_\infty$
HBR = high by-pass ratio
Ideal = referring to ideal flow conditions
Installed = referring to the installed configuration
Isolated = referring to the isolated configuration
k = turbulent kinetic energy, m^2/sec^2
LE & TE = leading edge and trailing edge
LP = low pressure
M and Re = Mach and Reynolds number
p and T = static pressure (Pa) and temperature (K)
P_0, T_0 = stagnation pressure (Pa) and temperature (K)
PS & SS = pressure side and suction side
q = dynamic head, Pa
R = air gas constant, J/(kg × K)
RMS = root mean square
Ram = referring to ram flow conditions
Throat = referring to the nozzle throat
V_x = axial velocity, m/sec
VHBR = very high by-pass ratio
y^+ = non-dimensional wall distance
γ = specific heat capacity ratio
κ = thermal conductivity, J/(m × K × sec)
λ = total to ambient static nozzle pressure ratio
ρ = flow density, kg/m^3
ω = specific dissipation rate, 1/sec
∞ = referring to ambient free-stream conditions

References

[1] Haselback, F., Newby, A., and Parker, R., 2015, "Next Generation of Large Civil Aircraft Engines - Concepts & Technologies," European Turbomachinery Conference, Madrid, Spain, Mar. 23–27.
[2] Epstein, A. H., 2014, "Aeropropulsion for Commercial Aviation in the Twenty-First Century and Research Directions Needed," AIAA J., **52**(5), pp. 901–911.
[3] Birch, N. T., 2000, "2020 Vision: The Prospects for Large Civil Aircraft Propulsion," Aeronaut. J., **104**(1038), pp. 347–352.
[4] Waters, M., and Schairer, E., 1977, "Analysis of Turbofan Propulsion System Weight and Dimensions," Ames Research Center, Moffet Field, CA, Report No. NASA TM X-73.
[5] Daggett, D. L., 2002, "Ultra Efficient Engine Technology Systems Integration and Environmental Assessment," Boeing Commercial Airplane Group, Seattle, WA, Report No. NASA/CR-2002-211754.
[6] Peters, A., Spakovsky, Z. S., Lord, W. K., and Rose, B., 2015, "Ultrashort Nacelles for Low Fan Pressure Ratio Propulsors," ASME J. Turbomach., **137**(2), p. 021001.
[7] Swarthout, A., MacManus, D., Matensanz-Garcia, J., Boscagli, L., and Sheaf, C., 2022, "A Comparative Assessment of Multiobjective Optimisation Methodologies for Aero-Engine Nacelles," ICAS 33rd Technical Congress, ICAS 2022-0162, Stockholm, Sweden, Sept. 4–9.
[8] Schreiner, N., Tejero, F., MacManus, D., and Sheaf, C., 2020, "Robust Aerodynamic Design of Nacelles for Future Civil Aero-Engines," ASME Paper No. GT2020-14470.

[9] Zachos, P. K., 2013, "Modelling and Analysis of Turbofan Engines Under Windmilling Conditions," J. Propul. Power, **29**(4), pp. 882–890.

[10] Rosa, N. G., Dufour, G., Barenes, R., and Lavergne, G., 2015, "Experimental Analysis of the Global Performance and the Flow Through a High-Bypass Turbofan in Windmilling Conditions," ASME J. Turbomach, **137**(5), p. 051001.

[11] Walsh, P., and Fletcher, P., 2004, *Gas Turbine Performance*, Blackwell Publishing, Oxford, UK.

[12] Goulos, I., Otter, J., Tejero, F., Rebassa, J.-H., MacManus, D., and Sheaf, C., 2021, "Civil Turbofan Propulsion Aerodynamics: Thrust-Drag Accounting and Impact of Engine Installation Position," Aerosp. Sci. Technol., **111**, p. 106533.

[13] Rao, A. N., Goulos, I., and MacManus, D., 2021, "Impact of Installation on a Civil Large Turbofan Exhaust System at Idle Descent Conditions," Aerosp. Sci. Technol., **119**, p. 107125.

[14] Subbian, G., Magrini, A., Buosi, D., Radespiel, R., Ponza, R., and Benini, E., 2021, "Investigation of HL-CRM Aerodynamics With a UHBPR Nacelle in Powered-on Condition," AIAA Paper No. 2021-3547.

[15] Subbian, G., Magrini, A., Benini, E., Buosi, D., Ponza, R., and Radespiel, R., 2022, "RANS Analysis of HL-CRM at Landing Configuration With Different Flap Deflections and Engine Representations," AIAA Paper No. 2022-0048.

[16] Robinson, M., MacManus, D. G., and Sheaf, C., 2018, "Aspects of Aero-Engine Nacelle Drag," Proc. Inst. Mech. Eng., Part G, **233**(5), pp. 1667–1682.

[17] Mattingly, J., 1996, *Elements of Gas Turbine Propulsion* (McGraw-Hill Series in Mechanical Engineering), McGraw-Hill, New York, Vol. 1.

[18] Goulos, I., Stankowski, T., Otter, J., MacManus, D., Grech, N., and Sheaf, C., 2016, "Aerodynamic Design of Separate-Jet Exhausts for Future Civil Aero-Engine, Part 1: Parametric Geometry Definition and CFD Approach," ASME J. Eng. Gas Turbines Power, **138**(8), p. 081201.

[19] Goulos, I., Otter, J., Stankowski, T., MacManus, D., Grech, N., and Sheaf, C., 2016, "Aerodynamic Design of Separate-Jet Exhausts for Future Civil Aero-Engines, Part 2: Surrogate Modeling and Optimization," ASME J. Eng. Gas Turbines Power, **138**(8), p. 081202.

[20] Goulos, I., Otter, J., Stankowski, T., MacManus, D., Grech, N., and Sheaf, C., 2018, "Design Optimisation of Separate-Jet Exhausts for the Next Generation of Civil Aero-Engines," Aeronaut. J., **122**(1256), pp. 1586–1605.

[21] Otter, J., Goulos, I., MacManus, D., and Slaby, M., 2018, "Aerodynamic Analysis of Civil Aero-Engine Exhaust Systems Using Computational Fluid Dynamics," J. Propul. Power, **34**(5), pp. 1152–1165.

[22] Giangaspero, G., MacManus, D., and Goulos, I., 9 2019, "Surrogate Models for the Prediction of the Aerodynamic Performance of Exhaust Systems," Aerosp. Sci. Technol., **92**, pp. 77–90.

[23] Otter, J. J., Stańkowski, T., Robinson, M., and MacManus, D. G., 2019, "Installation Aerodynamics of Civil Aero-Engine Exhaust Systems," Aerosp. Sci. Technol., **89**, pp. 345–355.

[24] Oliveira, G. L., Trapp, L. G., and Puppin-Macedo, A., "Integration Methodology for Regional Jet Aircraft With Underwing Engines," AIAA Paper No. 2003-934.

[25] Vassberg, J. C., Dehaan, M. A., Rivers, M. B., and Wahls, R. A., 2008, "Development of a Common Research Model for Applied CFD Validation Studies," AIAA Paper No. 2008-6919.

[26] Otter, J. J., Goulos, I., Christie, R., and MacManus, D. G., 2020, "Design and Analysis of Non-Axisymmetric Installed Aero-Engine Exhaust Systems," Aerosp. Sci. Technol., **106**, p. 106210.

[27] Gunn, E. J., and Hall, C. A., 2016, "Loss and Deviation in Windmilling Fans," ASME J. Turbomach., **138**(10), p. 101002.

[28] Ferrer-Vidal, L. E., Iglesias-Pérez, A., and Pachidis, V., 2020, "Characterization of Axial Compressor Performance at Locked Rotor and Torque-Free Windmill Conditions," Aerosp. Sci. Technol., **101**, p. 105846.

[29] Ferrer-Vidal, L. E., Pachidis, V., and Tunstall, R. J., 2021, "Generating Axial Compressor Maps to Zero Speed," Proc. Inst. Mech. Eng., Part A, **235**(5), pp. 956–973.

[30] Ferrer-Vidal, L. E., and Pachidis, V., 2021, "Numerical Modeling of Core Compressor Discharge for a Windmilling Aero Engine," Aerosp. Sci. Technol., **108**, p. 106365.

[31] Greenwell, D. I., 2022, "Transonic Industrial Wind Tunnels Testing in the 2020s," Aeronaut. J., **126**(1295), pp. 125–151.

[32] Mikkelsen, K. L., Myren, D. J., Dahl, D. G., and Christiansen, M. D., 2015, "Initial Subscale Performance Measurements of the AIAA Dual Separate Flow Reference (DSFR) Nozzle," AIAA Paper No. 2015-3883.

[33] ANSYS, 2017, *ANSYS FLUENT Theory Guide: Release 17.1*, ANSYS Inc., Canonsburg, PA.

[34] Ansys Inc., 2017, *ANSYS WORKBENCH User's Guide*, 275 Technology Drive, Canonsburg, PA.

[35] ANSYS Inc., 2013, *ANSYS FLUENT Theory Guide: Release 16.2*, ANSYS, Canonsburg, PA.

[36] Wilcox, D. C., 1993, "Comparison of Two-Equation Turbulence Models for Boundary Layers With Pressure Gradient," AIAA J., **31**(8), pp. 1414–1421.

[37] Sutherland, W., 1893, "The Viscosity of Gases and Molecular Forces," Philos. Mag., **36**(223), pp. 507–531.

School of Aerospace, Transport and Manufacturing (SATM)   Staff publications (SATM)

2024-02-01

Impact of installation on the performance of an aero-engine exhaust at wind-milling flow conditions

Goulos, Ioannis

American Society of Mechanical Engineers